JGR Atmospheres

RESEARCH ARTICLE
10.1029/2023JD039608

Key Points:

- The typical synoptic patterns (SPs) triggering summer extreme rainfall (Rx) are differed by mid-latitudes disturbances
- The connection between long-term changes in circulation and Rx emerges when considering various trends of different typical SPs
- Based on the model's capability to capture the typical SPs, a weighting method could narrow the inter-model spread of future projections

Correspondence to:
Y. Lin,
yanluan@tsinghua.edu.cn

Citation:
Hu, Y., Lin, Y., Deng, Y., & Bao, J. (2023). Summer extreme rainfall over the middle and lower reaches of Yangtze River: Role of synoptic patterns in historical changes and future projections. *Journal of Geophysical Research: Atmospheres*, *128*, e2023JD039608. https://doi.org/10.1029/2023JD039608

Received 7 JUL 2023
Accepted 27 NOV 2023

Summer Extreme Rainfall Over the Middle and Lower Reaches of Yangtze River: Role of Synoptic Patterns in Historical Changes and Future Projections

Yang Hu[1,2], Yanluan Lin[1], Yi Deng[3], and Jiawei Bao[4]

[1]Department of Earth System Science, Ministry of Education Key Laboratory for Earth System Modeling, Institute for Global Change Studies, Tsinghua University, Beijing, China, [2]Hubei Key Laboratory for Heavy Rain Monitoring and Warning Research, Institute of Heavy Rain, China Meteorological Administration, Wuhan, China, [3]School of Earth and Atmospheric Sciences, Georgia Institute of Technology, Atlanta, GA, USA, [4]Max Planck Institute for Meteorology, Hamburg, Germany

Abstract It is one of the major challenges in climate science to project future changes in extreme rainfall. To overcome this challenge, in this study, four typical synoptic patterns (SPs) triggering summer extreme rainfall over the middle and lower reaches of Yangtze River (MLYR) are identified through hierarchical clustering. These typical SPs share common characteristics of intensified Mei-yu trough and Western Pacific Subtropical High but differ in terms of mid-latitudes disturbances, such as an intensified ridge (Cluster 1, Cluster 2) or trough (Cluster 3, Cluster 4) near Lake Baikal (Cluster 1, Cluster 3) or Northeast China (Cluster 2, Cluster 4). The linkage between extreme rainfall and typical SPs is verified at various time scales. The typical SPs associated with extreme rainfall are substantially different from the circulation patterns found on ordinary days, and their frequency is significantly correlated with that of extreme rainfall across the interannual scales. Furthermore, the distinct changes in different typical SPs serve as a "bridge" for understanding the long-term impact of circulation changes on local extreme rainfall, even though the two do not appear to be connected at first sight. Specifically, the circulation changes imply more (less) frequent SP-Cluster 1 (SP-Cluster 3), which tends to produce more extreme rainfall to the south (north) of the Yangtze River within MLYR. To project future changes in extreme rainfall, we utilize a weighting method for the multi-model ensemble based on each model's capability to capture the observed typical SPs. This method effectively narrows the inter-model spread.

Plain Language Summary Extreme rainfall has a huge impact on human society and ecosystem, but the large uncertainty of extreme rainfall simulation hinders the use of climate models in future risk assessment. To reduce the uncertainty, we identify critical physical mechanisms for extreme rainfall formation in the real world and then utilize them as metrics to assess climate models and give more weight to models with better performances. We first identified four types of weather configurations as the critical physical mechanisms for extreme rainfall formation, which are further verified to be closely connected with extreme rainfall at different time scales (i.e., daily, interannual, and several decades). Then, we assess how well each model captures these weather configurations and then generate weighted multi-model ensembles based on the model performances. This method effectively reduces the uncertainty in future projections. This assessment and correction procedure has great potential to provide reliable projections of extreme events in other regions and seasons.

1. Introduction

Extreme rainfall is among the most destructive natural disasters due to its impact on human society and ecosystem. The middle and lower reaches of Yangtze River (MLYR; Figure 1a) often suffer from extreme rainfall, especially during June and July (i.e., Mei-yu season) when the East Asian summer monsoon produces intense rainfall (Ding & Chan, 2005). As this region is densely populated, it makes them vulnerable to extreme rainfall. It is therefore crucial to understand how summer extreme rainfall over MLYR varied in the past and how it will change in the future.

Extreme rainfall in the mid-latitudes often requires favorable synoptic patterns (SPs) that can enhance moisture transport, adiabatic ascent, and orographic lifting (Barlow et al., 2019; Chen & Zhai, 2015; Dai & Nie, 2020; Sampe & Xie, 2010; X. Xu, Huang, et al., 2023; C. Zhang et al., 2021; S. Zhang et al., 2022; Zhao et al., 2017; Zhu et al., 2023). Therefore, the SPs concurrent with extreme rainfall (i.e., typical SPs) have been identified and

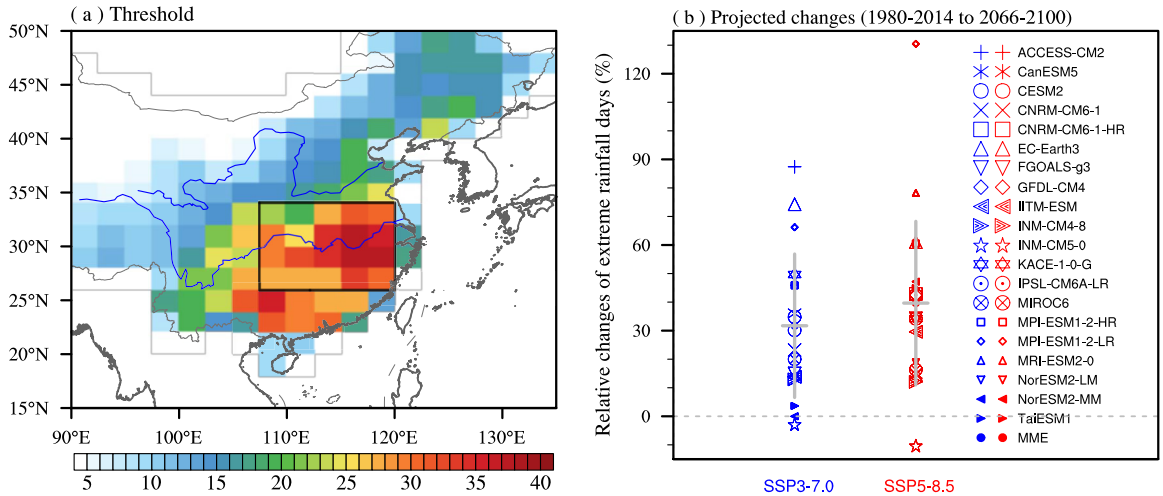

Figure 1. (a) The threshold (units: mm) of local extreme daily rainfall in observations and the domain of the middle and lower reaches of Yangtze River (MLYR; black box). (b) Projected relative changes (units: %; 2066–2100 relative to 1980–2014) in extreme rainfall days over MLYR in SSP3-7.0 (blue) and SSP5-8.5 (red) scenarios. The gray solid lines indicate one standard deviation of projected changes among CMIP6 models.

the frequency changes of typical SPs are found to play an important role in the observed trends of extreme rainfall (Prein & Mearns, 2021; Y. Tang et al., 2021). Other studies highlighted the combined effects of changes in favorable SP frequency and thermodynamic changes (i.e., rainfall intensity or water availability) during specific SP days (Davenport & Diffenbaugh, 2021; Ohba et al., 2022).

Models from the sixth phase of Coupled Model Intercomparison Project (CMIP6; Eyring et al., 2016) are primary tools to project future changes in extreme rainfall, but the credibility remains uncertain (Jiang et al., 2023; C. Li, Zwiers, et al., 2021; F. Li et al., 2022; H. Xu et al., 2021). Here we found that CMIP6 models generally projected increased extreme rainfall frequency over MLYR (see definition in Section 2.2.1) under two Shared Socioeconomic Pathways (SSP; i.e., SSP3-7.0 and SSP5-8.5; O'Neill et al., 2016). But the CMIP6 projections have a large inter-model spread on the magnitude (Figure 1b), consistent with the large inter-model spread of projected extreme rainfall over eastern China (C. Li, Zwiers, et al., 2021; H. Xu et al., 2021).

Considering the diverse skills of CMIP6 models in reproducing present-day rainfall statistics, one way is to utilize weighted multi-model ensemble (MME) to constrain future projections. The weights are generated by assessing model performance in historical rainfall simulations (Brunner et al., 2019; Gründemann et al., 2022; W. Li et al., 2016; B. Tang et al., 2021; Zhao et al., 2022) or simultaneously assessing model performance in capturing key processes for rainfall variability, for example, the relationship between rainfall and large-scale monsoon index (Wang et al., 2021) or teleconnection patterns between rainfall and sea level pressure over specific oceanic regions (F. Li et al., 2022). Given the close connection between extreme rainfall and typical SPs and the higher skills in simulating SPs for CMIP5/6 models (compared with extreme rainfall simulation), changes in typical SPs can be used as a proxy to infer extreme rainfall changes (Gao et al., 2017). Indeed, Gao et al. (2017) found a smaller inter-model spread of projected changes in extreme rainfall as inferred from the typical SP than that of rainfall directly from the model. However, some studies suggested that CMIP5/6 models have diverse ability to reproduce the observed characteristics of SPs associated with extreme events (Agel & Barlow, 2020; Agel et al., 2020; Loikith & Broccoli, 2015) or the spectrum of SPs spanning the entire period (Gibson, Perkins-Kirkpatrick, et al., 2016, Gibson, Uotila, et al., 2016; Taylor et al., 2023). Previous studies identified typical SPs associated with extreme rainfall over the middle reaches of Yangtze River and found consistent bias direction between these typical SPs and rainfall (Hu, Deng, Zhou, Cui, & Dong, 2019, Hu, Deng, Zhou, Li, et al., 2019). Therefore, the inter-model spread of extreme rainfall may be partly attributed to the inter-model spread of its synoptic drivers. It is imperative to assess the credibility of CMIP6 models in triggering extreme rainfall over MLYR and correct projected changes based on their historical performance, which has not been done yet. This work further verifies the linkage between extreme rainfall and the typical SPs through statistical analysis, that is, the separation of circulation patterns on extreme rainfall days and ordinary days, the role of typical SPs in interannual variations and long-term trends of extreme rainfall frequency. Then we show that a typical-SPs-based-weighting method can narrow the inter-model spread and decrease the MME mean of projected changes in extreme rainfall over MLYR.

Table 1
Model Name, Institution, Atmospheric Resolution Around the Study Domain (Latitude × Longitude) and the Rank-Based Weight (W_i; Units: %) of 20 CMIP6 Models

Model name	Institution	Resolution	Weight (W_i)
ACCESS-CM2	CSIRO (Commonwealth Scientific and Industrial Research Organisation), Australia	1.250 × 1.875°	3.474
CanESM5	CCCma (Canadian Centre for Climate Modelling and Analysis), Canada	2.791 × 2.813°	1.463
CESM2	NCAR (National Center for Atmospheric Research), US	0.942 × 1.250°	5.559
CNRM-CM6.1	CNRM-CERFACS (Centre National de Recherches Météorologiques-Centre Europeen de Recherche et Formation Avancees en Calcul Scientifique), France	1.401 × 1.406°	2.527
CNRM-CM6.1-HR		0.500 × 0.500°	3.088
EC-Earth3	EC-Earth-Consortium	0.702 × 0.703°	2.780
FGOALS-g3	IAP (Institute of Atmospheric Physics), China	2.025 × 2.000°	13.898
GFDL-CM4	GFDL (Geophysical Fluid Dynamics Laboratory), US	2.000 × 2.500°	1.635
IITM-ESM	IITM (Indian Institute of Tropical Meteorology), India	1.905 × 1.875°	4.633
INM-CM4.8	INM (Institute for Numerical Mathematics), Russia	1.500 × 2.000°	1.544
INM-CM5.0		1.500 × 2.000°	1.390
IPSL-CM6A-LR	IPSL (Institut Pierre Simon Laplace), France	1.268 × 2.500°	3.971
KACE-1-0-G	NIMS/KMA (National Institute of Meteorological Sciences/Korea Meteorological Administration), Korea	1.250 × 1.875°	2.138
MIROC6	CCSR/UT/JAMSTEC/NIES (Center for Climate System Research/University of Tokyo/Japan Agency for Marine-Earth Science and Technology/National Institute for Environmental Studies), Japan	1.401 × 1.406°	1.853
MPI-ESM1.2-HR	MPI (Max Planck Institute), Germany	0.935 × 0.938°	2.316
MPI-ESM1.2-LR		1.865 × 1.875°	1.737
MRI-ESM2.0	MRI (Meteorological Research Institute), Japan	1.121 × 1.125°	6.949
NorESM2-LM	NCC (Norwegian Climate Centre), Norway	1.895 × 2.500°	27.795
NorESM2-MM		0.942 × 1.250°	1.985
TaiESM1	AS-RCEC (Academia Sinica-Research Center for Environmental Changes), Taiwan, China	0.942 × 1.250°	9.265

2. Data and Methods

2.1. Data

Two observational data sets are used. For daily precipitation over China, we use a gridded (0.25° × 0.25°) data set (CN05.1) covering the period from 1961 to 2021, which is constructed with more than 2400 station observations in the mainland China (Wu & Gao, 2013). The daily atmospheric variables (i.e., geopotential height and horizontal winds) with a resolution of 1.0° × 1.0° from 1961 to 2021 are calculated using the latest reanalysis (ERA5) from the European Centre for Medium-Range Weather Forecasts (Hersbach et al., 2023). The period of 1961–2021 covers both the analysis period (i.e., 1980 to 2021) and the out-of-sample test period (i.e., 1961 to 1979). The out-of-sample test are performed to assess whether the relationship between extreme rainfall and typical SPs extends beyond the analysis period when the two are defined. The circulations in reanalysis data will be labeled "observed" to distinguish them from the CMIP6 outputs. 20 CMIP6 models that provide daily precipitation and geopotential height in the historical experiment and two future scenarios with high emission (i.e., SSP3-7.0 and SSP5-8.5) are used for synoptic assessment and future projections (Table 1). In general, we use the first ensemble member (i.e., r1ip1f1) of each model. But if the first ensemble member is not provided, we use the other ensemble member (e.g., using r1i1p1f1 for CESM2; using r1i1p1f2 for CNRM-CM6.1 and CNRM-CM6.1-HR).

2.2. Methods

2.2.1. Extreme Rainfall Days Within MLYR

For a fair comparison between observations and CMIP6 models, the observed and modeled rainfall are remapped to the 2.0°(latitude) × 2.5° (longitude) grids (see Figure 1a) using an area-conserving method. The local extreme rainfall threshold of each grid is defined as the 95th percentile of daily rainfall for all days during the Mei-yu season (June and July) from 1980 to 2021. All wet and dry days are included in calculating the threshold

considering the different rainfall frequencies between observations and CMIP6 models. The MLYR region (26–34°N, 107.5–120°E; the black box in Figure 1a) generally has higher extreme rainfall thresholds (Figure 1a). The extreme rainfall days within MLYR are detected when more than 25% grids in the MLYR exceed their extreme rainfall thresholds. The extreme rainfall days in CMIP6 models are selected based on their own historical thresholds from 1980 to 2014. The relative changes of extreme rainfall frequency are calculated by changes in projection period (2066–2100) relative to that in historical period (1980–2014).

2.2.2. Identification of Typical SPs

Previous studies suggest that extreme rainfall within MLYR is closely related to low-level circulations (Hu, Deng, Zhou, Cui, & Dong, 2019, Hu, Deng, Zhou, Li, et al., 2019). Here the daily geopotential height at 700 hPa covering China (15–55°N, 85–135°E) from 1980 to 2021 is used to objectively identify extreme-rainfall-triggering-SPs through hierarchical clustering (Hu, Deng, Zhou, Cui, & Dong, 2019, Hu, Deng, Zhou, Li, et al., 2019; Zhao et al., 2016). Extreme rainfall during the Mei-yu season has evident diabatic feedback on Mei-yu fronts (Hu et al., 2021, 2022) and thus could modify the low-level circulations. As a result, the consecutive extreme rainfall days are considered as a single extreme rainfall event and only the circulations on the starting days of consecutive extreme rainfall days are used. We exclude the days influenced by tropical cyclones (TC) over the Western North Pacific Ocean because of the potential feedback of TC to circulations. Here we have identified 102 extreme rainfall days in observations from 1980 to 2021. As the first step of hierarchical clustering, the circulation pattern (i.e., daily total geopotential height at 700 hPa) associated with each extreme rainfall day is regarded as a singleton cluster; in subsequent steps, two clusters with the smallest dissimilarity (represented by Ward's distance; Ward, 1963) are merged until an evident "jump" in the smallest Ward's distance emerges. This "jump" indicates quite different clusters are merged and the merging process should be terminated. Following this procedure (figure not shown), we identified four typical SPs triggering extreme rainfall over MLYR in observations.

2.2.3. Frequency of Typical SPs Days

Days that have similar circulation patterns to any of the typical SPs are identified as typical SPs days. First, the similarity of daily circulation to a typical SP is measured by the spatial correlation coefficient (COR) and root mean squared error (RMSE) between the daily circulation and the mean circulation of a typical SP. Then, typical SPs days are identified when the daily CORs (RMSEs) are higher (lower) than the lower-limits (upper-limits) of the 95% confidence interval of mean COR (RMSE) from extreme rainfall days associated with the corresponding cluster.

2.2.4. The Synoptic Assessment and Rank-Based Weighting

We first assess how well the SPs triggering extreme rainfall in CMIP6 models fit the typical SPs identified in observations. Then we adopted a rank-based weighting method (W. Li et al., 2016) to constrain future projections.

The modeled geopotential height is interpolated to the same 2.0° × 2.5° grids using bilinear interpolation, and typical SPs in models are obtained by clustering the modeled geopotential height at 700 hPa. The cluster number of typical SPs in models is set to four for easy comparison between observed and modeled typical SPs. Each typical SP in CMIP6 models triggering modeled extreme rainfall is assigned to the most similar SP in observations based on the spatial correlation coefficients (i.e., assigned to the observed SP with the maximum correlation coefficient). The capability (C_i) of each CMIP6 model to capture the observed typical SPs is measured by the sum of the four correlation coefficients between modeled typical SPs and the assigned SPs in observations, weighted by the occurrence frequency of the modeled SPs. Then a rank-based skill index (S_i) of each model is defined as:

$$S_i = \frac{\sum_{i=1}^{N} R_i}{R_i}, \tag{1}$$

where R_i is the rank of a model' capability (C_i) to capture the observed typical SPs. Finally, the weight (W_i) of each model, which is used to constrain future projections, is obtained as a function of the rank-based skill index (S_i):

$$W_i = \frac{S_i}{\sum_{i=1}^{N} S_i}. \tag{2}$$

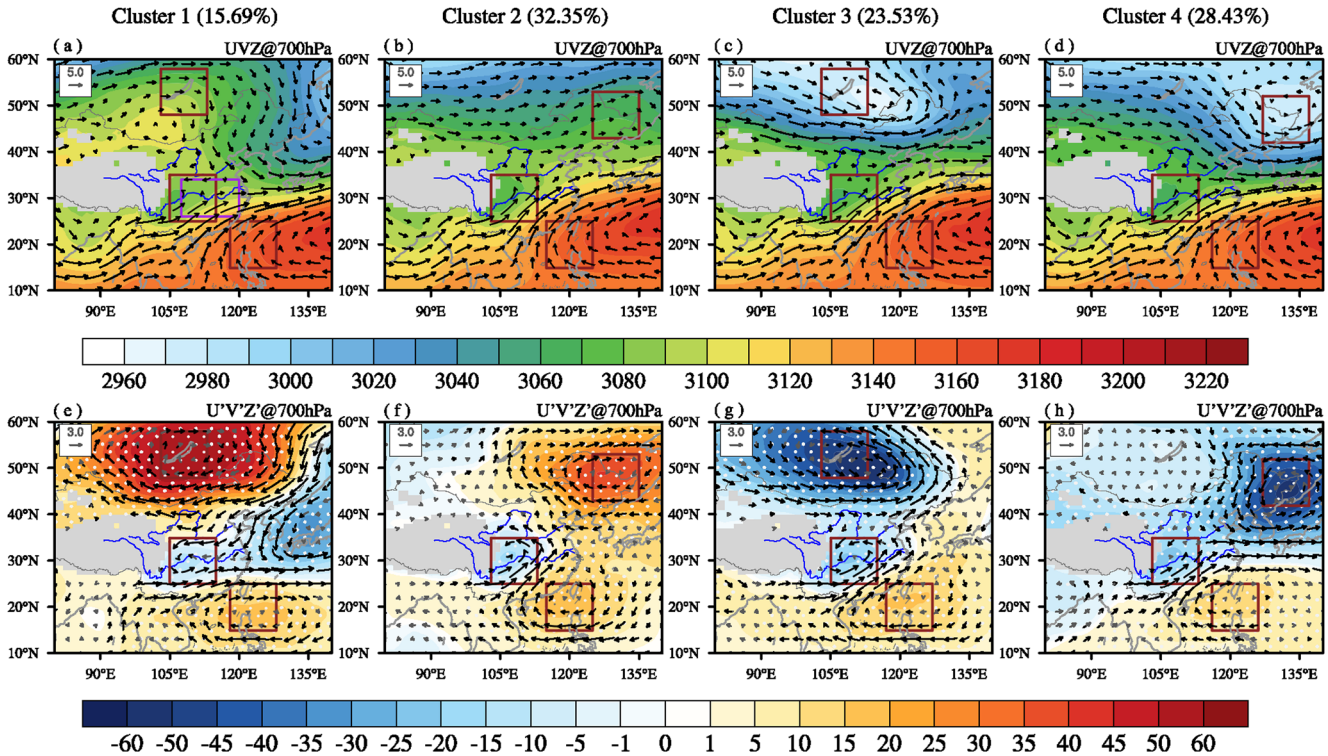

Figure 2. (a–d) The cluster-mean geopotential height (Z; shading; units: gpm) and horizontal winds (UV; vectors; units: m s^{-1}) and (e–h) cluster-mean anomaly of geopotential height (Z′) and horizontal winds (U′V′) at 700 hPa. The significant geopotential height and wind anomalies are highlighted by white dots and black vectors ($p < 0.1$). The brown boxes indicate the critical locations of each typical synoptic pattern.

3. Results

3.1. Typical SPs Triggering Extreme Rainfall

The typical SPs triggering extreme rainfall are shown in Figures 2a–2d. Four clusters share common features of an intensified Mei-yu trough around the middle reaches of Yangtze River (25–35°N, 105–120°E), and a westward-extended and intensified Western Pacific Subtropical High (WPSH) over South China Sea (15–25°N, 115–128°E). The major differences among the clusters are the synoptic disturbances near two critical locations at mid-latitudes. Specifically, SP-Cluster 1 (SP-Cluster 3) is characterized by a strong ridge (trough) near Lake Baikal (48–58°N, 103–113°E), while SP-Clusters 2 (SP-Cluster 4) is associated with a strong ridge (trough) near Northeast China (42–53°N, 125–137°E). This is consistent with recent studies suggesting that the East Asia summer rainfall is closely related to mid- and high-latitude disturbances, in addition to anomalies over the subtropical and tropical western North Pacific (Chen et al., 2023; Hu, Deng, Zhou, Cui, & Dong, 2019; X. Li & Lu, 2017; J. Li, Zwiers, et al., 2021; X. Li et al., 2023; Z. Xu, Huang, et al., 2023). Therefore, each typical SP has three critical locations at subtropical, extratropical and mid-latitude regions (Figures 2a–2d). The synoptic anomalies are more evident by removing the multi-year calendar-day mean (Figures 2e–2h). Associated with these circulation patterns, significant anomalies of low-level convergence and deformation are found ahead of the Mei-yu front (Figures 3i–3l; the definition of Mei-yu front line is provided in the Appendix). These anomalies could enhance Mei-yu frontogenesis along the Yangtze River, thus favoring the frontal ascent motion and convection initiation (F. Zhang et al., 2023). In addition, the low-level ascent along the Yangtze River is coupled with the ascent favored by upper-level and mid-level circulations (Figures 3a–3h). Specifically, the South Asia High moves eastward in Cluster 1, Cluster 2 and Cluster 3, resulting in the eastward movement of the ridge line. The upper-level westerly jet accelerates to the northeast of MLYR in Cluster 1, Cluster 2 and Cluster 4, forming a right entrance region of the upper-level jet above MLYR. These patterns could produce a positive vorticity advection anomaly at upper-levels, which favors upper-level divergence and adiabatic ascent around MLYR (Figures 3a–3d). The strengthened mid-troposphere warm advection associated with the westerly flow anomaly also enhances the mid-level ascent (Figures 3e–3h).

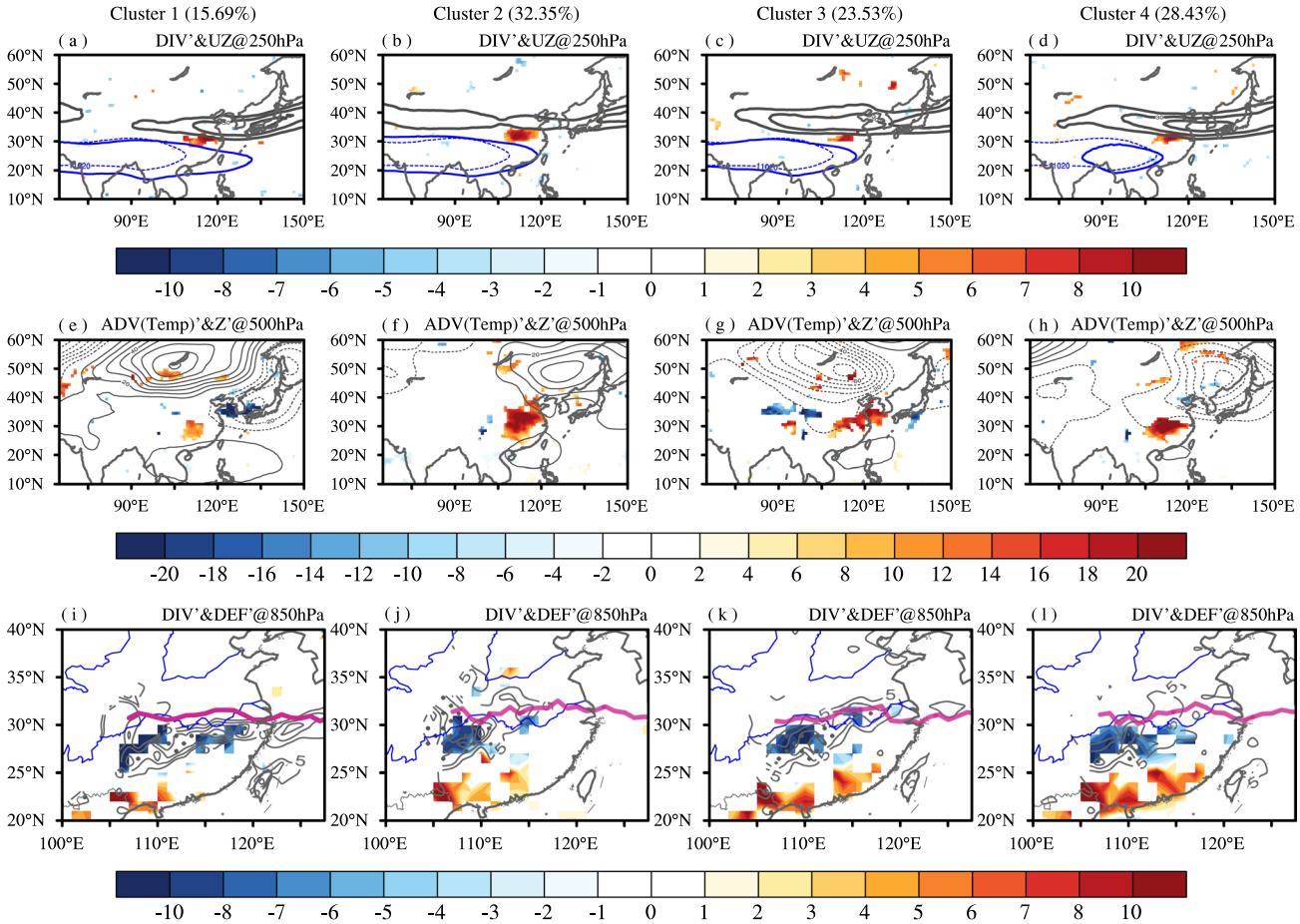

Figure 3. (a–d) The cluster-mean geopotential height (Z; blue solid contours; units: gpm), zonal wind velocity (U; black contours; units: m s^{-1}), and cluster-mean anomaly of divergence (DIV'; shading; units: 10^{-6} s^{-1}; only significant anomaly is shown, $p < 0.1$) at 250 hPa of each cluster. The climatology geopotential height is shown in blue dashed contours. (e–h) The cluster-mean anomaly of horizontal temperature advection (ADV(temp)'; shading; units: 10^{-6} K s^{-1}; only significant anomaly is shown, $p < 0.1$) and geopotential height (Z'; black contours; units: gpm) at 500 hPa of each cluster. (i–l) The cluster-mean anomaly of divergence (shading; units: 10^{-6} s^{-1}, only significant anomaly is shown, $p < 0.1$) and deformation (DEF'; gray contours; units: 10^{-6} s^{-1}, the significant anomaly is highlighted by gray dots) at 850 hPa. The mean locations of Mei-yu front line are indicated by purple lines.

3.2. Verification of the Linkage With Extreme Rainfall

To verify the importance of typical SPs on extreme rainfall over MLYR, we reconstruct the rainfall using the correlation between daily rainfall and typical SPs. First, we measure the similarity of daily circulations to a typical SP by the spatial correlation coefficients (CORs) between the daily circulations and the mean circulation of a typical SP. Second, we calculate the regression coefficient (REG) of daily rainfall at each grid against daily CORs for a typical SP during all days within the Mei-yu season from 1980 to 2021. A significant positive value of REG at a grid indicates that local daily rainfall increases rapidly as the corresponding daily circulation bears higher similarity to a typical SP. Finally, we reconstruct the daily rainfall at each grid by multiplying the REG and the mean COR in extreme rainfall days for a typical SP. This provides an estimate of the daily rainfall when a typical SP emerges. It is found that the reconstructed rainfall indeed exhibits higher rainfall intensities within MLYR (Figures 4a–4d), compared with other regions. This suggests a higher potential for typical SPs producing extreme rainfall over there. Furthermore, the spatial distribution of the reconstructed rainfall also resembles that of the cluster-mean rainfall in observations (Figures 4i–4l). The correlation coefficients between the reconstructed and observed rainfall within the MLYR are 0.71, 0.68, 0.94, and 0.72 ($p < 0.01$) for the four clusters respectively. Similar results can be found when the REGs are calculated using daily rainfall against daily RMSEs for a typical SP (Figures 4e–4h). Although the reconstructed and observed daily rainfall share similar spatial patterns, the magnitude of reconstruction is lower than observations, especially for the reconstruction using the regression

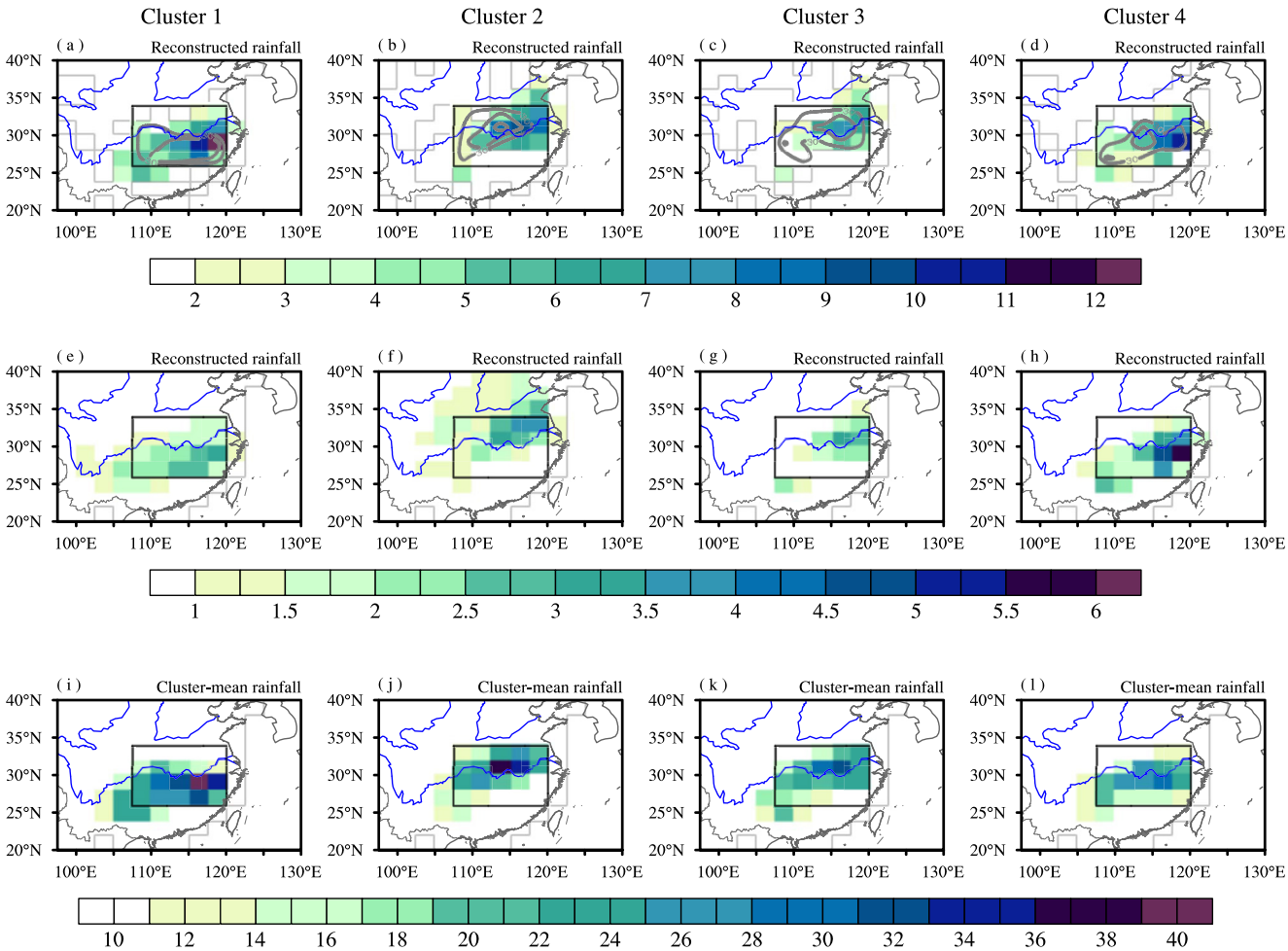

Figure 4. Reconstructed daily rainfall intensity (shading; units: mm; see text for definition) based on the regression against (a–d) daily COR and (e–h) daily root mean squared error for each cluster. Only the reconstructed rainfall associated with significant regression coefficient ($p < 0.1$) is shown. The occurrence frequency (units: %) of local extreme rainfall within each cluster is indicated by gray contours in panels (a–d). (i–l) The cluster-mean daily rainfall intensity in observations for each cluster (units: mm).

against RMSE. This implies that other factors such as convection intensify local rainfall. Generally, these results verify the importance of typical SPs to extreme rainfall formation over MLYR.

The sensitivity of the sub-regions to the four typical SPs shows distinct geographical differences. For instance, the reconstructed rainfall using SP-Cluster 1 is mainly confined to the south of the Yangtze River (shading in Figure 4a). For extreme rainfall days triggered by SP-Cluster 1, the southern part within MLYR also has a higher occurrence frequency of extreme rainfall compared with the northern part (gray contours in Figure 4a). This southern-centered feature of rainfall distribution is consistent with that of cluster-mean rainfall in Cluster 1 (Figure 4i). SP-Cluster 1 is thus more inclined to produce local extreme rainfall to the south of the Yangtze River within MLYR. Additionally, SP-Cluster 2 and SP-Cluster 3 (SP-Cluster 4) are more inclined to produce extreme rainfall slightly to the north (south) of the Yangtze River within MLYR (Figures 4b–4d, 4f–4h, 4j–4l).

Furthermore, the typical SPs corresponding to extreme rainfall events are significantly different from circulation patterns on ordinary days that do not necessarily produce extreme rainfall (Figure 5). Specifically, the probability of high COR from extreme rainfall events is higher than that from ordinary days and the upper-limit (95%) of random probability. Here the upper-limit is estimated using a Monte Carlo approach with 5,000 trials. Each trial is performed using randomly selected days while remaining the same number of days as the extreme rainfall events. The probability distribution function of daily COR from extreme rainfall events has a narrower width (i.e., smaller variance) compared with that from ordinary or random days and generally converges on the

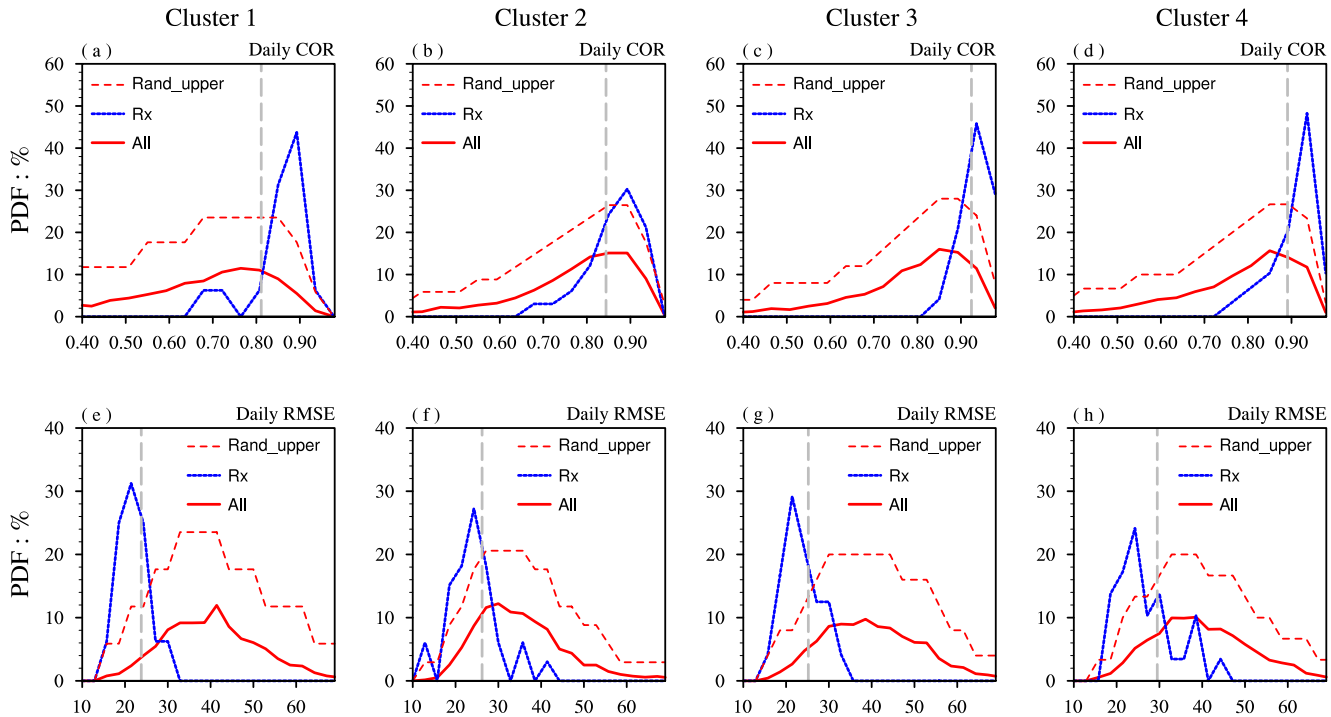

Figure 5. (a–d) The probability distribution function (PDF) of daily COR from extreme rainfall days (Rx; blue dashed lines) and all days (All; red solid lines). The red dashed lines delineate the upper-limit (95%) of random PDF (Rand_upper) using a Monte Carlo approach. The gray vertical lines in indicate the 95% confidence interval of mean COR for extreme days of each cluster. (e–h) The same as (a–d) but for daily root mean squared error.

high COR tail. Consistently, even the lower-limits of the 95% confidence interval of mean COR for extreme rainfall events of four clusters reach 0.81, 0.84, 0.92, and 0.89 (Figures 5a–5d). Likewise, the probability of low RMSE from extreme rainfall events is higher than that of ordinary days and the upper-limit of random probability (Figures 5e–5h). And the upper-limits of the 95% confidence interval of mean RMSE from extreme rainfall events of four clusters are 23.78, 26.19, 25.21, and 29.47 (Figures 5e–5h).

3.3. Interannual Variations and Long-Term Trends

We further verify the role of typical SPs on extreme rainfall over MLYR by evaluating their interannual variations. The annual frequency of extreme rainfall and the total annual frequency for the four typical SPs from 1980 to 2021 are displayed in Figure 6. The statistically significant ($p < 0.01$) correlation between the annual frequency of typical SPs and extreme rainfall over MLYR corroborates the critical role of typical SPs in driving extreme rainfall formation. Additionally, we evaluate their relationship from 1961 to 1979. This serves as an out-of-sample test since it is beyond the period when extreme days and typical SPs are identified. The out-of-sample test also indicates that the typical SPs and extreme rainfall are significantly correlated (Figure 6; shaded region).

Here we present the impact of typical SPs on extreme rainfall in terms of long-term trends. Our results show that although long-term trends are weak (Figure 6), a dissection of the typical SPs frequency into four clusters reveals distinct trends across the clusters (Figure 7). Specifically, the frequency of SP-Cluster 1, which accounts for 12.20% of all typical SPs days, exhibits a significant positive trend (4.24 decade^{-1}). However, this is offset by a significant negative trend (−3.19 decade^{-1}) of SP-Cluster 3, which accounts for 20.20% of all typical SPs days. For SP-Cluster 2 (37.74%) and SP-Cluster 4 (29.86%), their trends are weak and insignificant. Furthermore, we analyzed the pattern intensity for each typical SP days, which is defined by the mean absolute value of relative vorticity over the three critical locations for each typical SP (brown boxes in Figure 2). The result indicates that the pattern intensity has negligible long-term changes (Figures 7a–7d). We also investigated the extreme rainfall intensity during typical SPs days, which is defined by the mean rainfall of the upper 25% grids within MLYR. Our result shows that the extreme rainfall intensity for Cluster 2, Cluster 3, and Cluster 4 (i.e., more than 87% of all typical SPs days) has weak long-term changes (Figures 7b–7d). Overall, our analysis suggests that the impact of

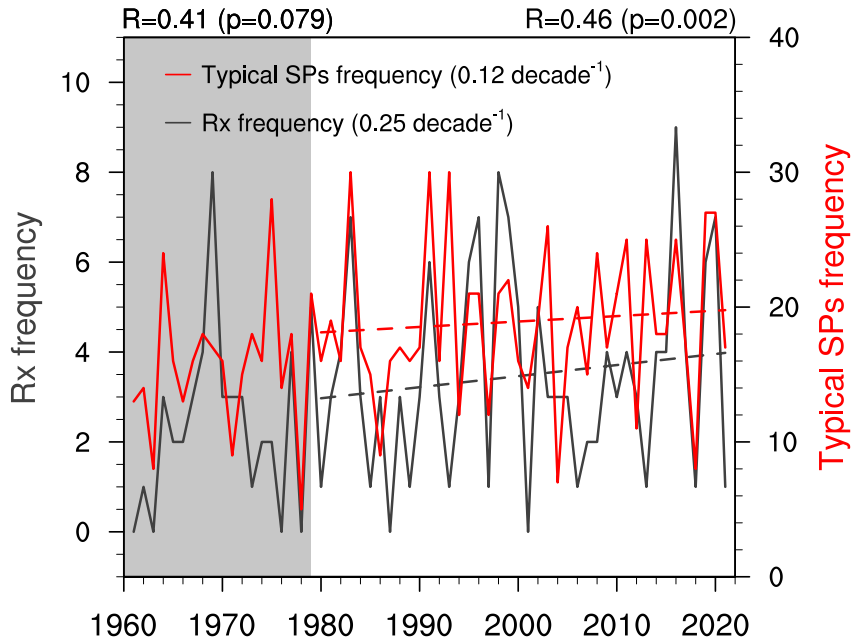

Figure 6. The annual frequency for the four typical synoptic patterns (SPs) (red solid lines) and the extreme rainfall (Rx; gray solid lines) over middle and lower reaches of Yangtze River from 1961 to 2021. The annual frequency for the out-of-sample test period (1961–1979) are highlighted in gray background. The correlation coefficient (R) between the frequency of typical SPs and extreme rainfall from 1980 to 2021 (1961–1979) is shown in the right (left) corner. The linear regression lines for long-term trends from 1980 to 2021 are represented by dashed lines and their values are shown in the parentheses (units: decade^{-1}).

typical SPs changes (i.e., frequency, pattern intensity, and extreme rainfall intensity changes) on extreme rainfall is limited. This is consistent with the weak trend of extreme rainfall days over MLYR.

The frequency of local extreme rainfall to the south of the Yangtze River within MLYR has more clear increasing long-term trends than those to the north (Figure 8a). It seems these long-term changes in extreme rainfall are not directly related to changes in summer-mean low-level circulation, which exhibit a significant increase of geopotential height and enhanced cyclonic flow near Lake Baikal (Figure 8b). Surprisingly, the circulation-rainfall connection emerges when considering the significant positive (negative) trend of SP-Cluster 1 (SP-Cluster 3). Specifically, the trend of circulation changes is consistent with (opposite to) the mid-latitude anomaly of SP-Cluster 1 (SP-Cluster 3), which implies more (less) frequent SP-Cluster 1 (SP-Cluster 3). As SP-Cluster 1 (SP-Cluster 3) tends to produce more extreme rainfall to the south (north) of the Yangtze River, the circulation changes tend to produce more frequent extreme rainfall to the south of the Yangtze River. To further illustrate that SP-Cluster 1 and SP-Cluster 3 serve as a "bridge" for understanding the impacts of circulation changes on local extreme rainfall, we reconstruct the circulation and extreme rainfall changes using the trends of SP-Cluster 1 and SP-Cluster 3 and their associated circulation (Figures 2e and 2g) and rainfall patterns (Figures 4a and 4c). For instance, the long-term trends of SP-Cluster 1 (i.e., 4.24 decade^{-1}) and SP-Cluster 3 (-3.19 decade^{-1}) are multiplied by their associated circulation anomaly pattern respectively to produce the circulation changes for SP-Cluster 1 and SP-Cluster 3. To reconstruct the circulation changes finally, we use a weighted sum of the circulation changes for SP-Cluster 1 and SP-Cluster 3, where the weights are determined by the frequency of SP-Cluster 1 and SP-Cluster 3 (i.e., 12.20% and 20.20% for SP-Cluster 1 and SP-Cluster 3, respectively). It is found that the spatial pattern of the reconstructed circulation changes (Figure 8d) is broadly consistent with that of the actual changes (Figure 8b). The spatial correlation coefficient between them is 0.78 ($p < 0.01$). Within MLYR, the reconstructed rainfall changes (Figure 8c) could capture the spatial pattern of frequency changes in extreme rainfall (Figure 8a), with a spatial correlation coefficient of 0.46 ($p < 0.05$). Note that the observed extreme rainfall changes outside MLYR are noisier than the reconstructed changes as the typical SPs defined here are mainly associated with extreme rainfall within MLYR. Also note that there is a relatively weak northerly flow anomaly over MLYR, which suggests a slightly weakened southerly monsoon flow and could displace the rain belt southward.

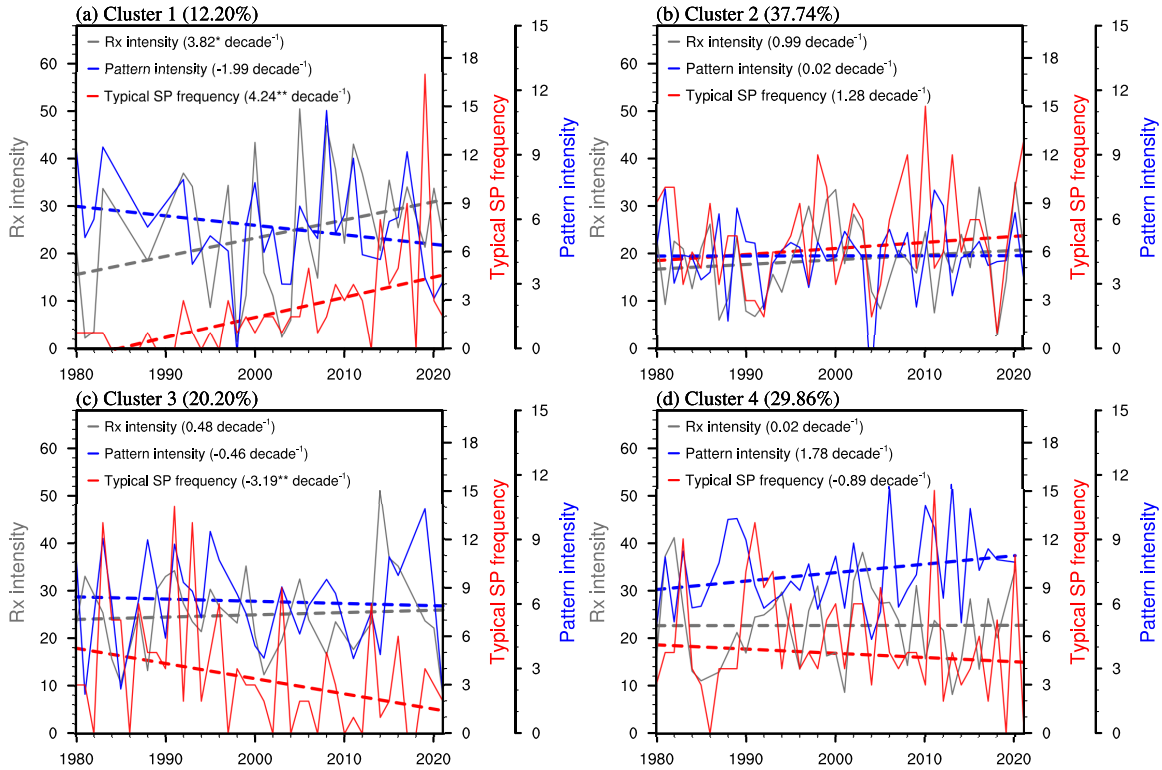

Figure 7. The annual frequency of each typical synoptic pattern (SP) (red solid lines), their annual mean pattern intensity (blue solid lines; units: 10^{-6} s^{-1}) and extreme rainfall (Rx) intensity over middle and lower reaches of Yangtze River (gray solid lines; units: mm). The occurrence frequency (units: %) of each typical SP relative to the four typical SPs is indicated in the parentheses in the upper-left corner. The dashed lines are linear regression lines for long-term trends from 1980 to 2021 and their values are shown in the parentheses (units: $decade^{-1}$). The statistically significant trends at the 0.1 level and the 0.05 level are indicated by * and **.

3.4. Constrained Future Projections

Given the importance of typical SPs in producing extreme rainfall, it is reasonable to have more confidence in models simulating more similar typical SPs in historical simulations as compared with the observations. Based on the rank-based weights of CMIP6 models' capability to capture the observed typical SPs (Table 1), we found that the projected changes of extreme rainfall in both scenarios can be constrained. Specifically, the model spread of projected changes in extreme rainfall frequency over MLYR can be reduced by 20.59% and 25.92% in the SSP3-7.0 and SSP5-8.5 scenarios, respectively (Figures 9a and 9b). The projected MME mean have a reduction of 8.43% and 3.58%, from the raw mean (31.72% and 39.65%) to the weighted mean (23.29% and 36.07%), in the SSP3-7.0 and SSP5-8.5 scenario, respectively (Figures 9a and 9b). Regarding the projected changes in local extreme rainfall frequency, the weighting method also reduces their standard deviation among models. The relative reduction within MLYR can reach 31.08% (35.04%) in the SSP3-7.0 (SSP5-8.5) scenario (Figures 9c and 9d). The raw MME mean exhibits positive trends of local extreme rainfall over MLYR. The weighting method increases the positive trends over the southeast part of MLYR while reduces it in the northwest part.

4. Summary and Discussion

In this study, we identify four typical SPs which tend to trigger extreme rainfall over MLYR during the Mei-yu season (June and July) from 1980 to 2021. These SPs share common characteristics of intensified Mei-yu trough and WPSH but differ in terms of an intensified ridge (Cluster 1, Cluster 2) or trough (Cluster 3, Cluster 4) near Lake Baikal (Cluster 1, Cluster 3) or Northeast China (Cluster 2, Cluster 4). These SPs could trigger extreme rainfall by enhancing ascent and convection along the Yangtze River. The linkage between SPs and extreme rainfall is verified at various time scales. (a) The typical SPs are substantially different from circulation patterns found on ordinary days. (b) The annual frequency of typical SPs is significantly correlated with that of the extreme rainfall within MLYR. (c) The long-term trends of SP-Cluster 1 and SP-Cluster 3 serve as a “bridge” for understanding

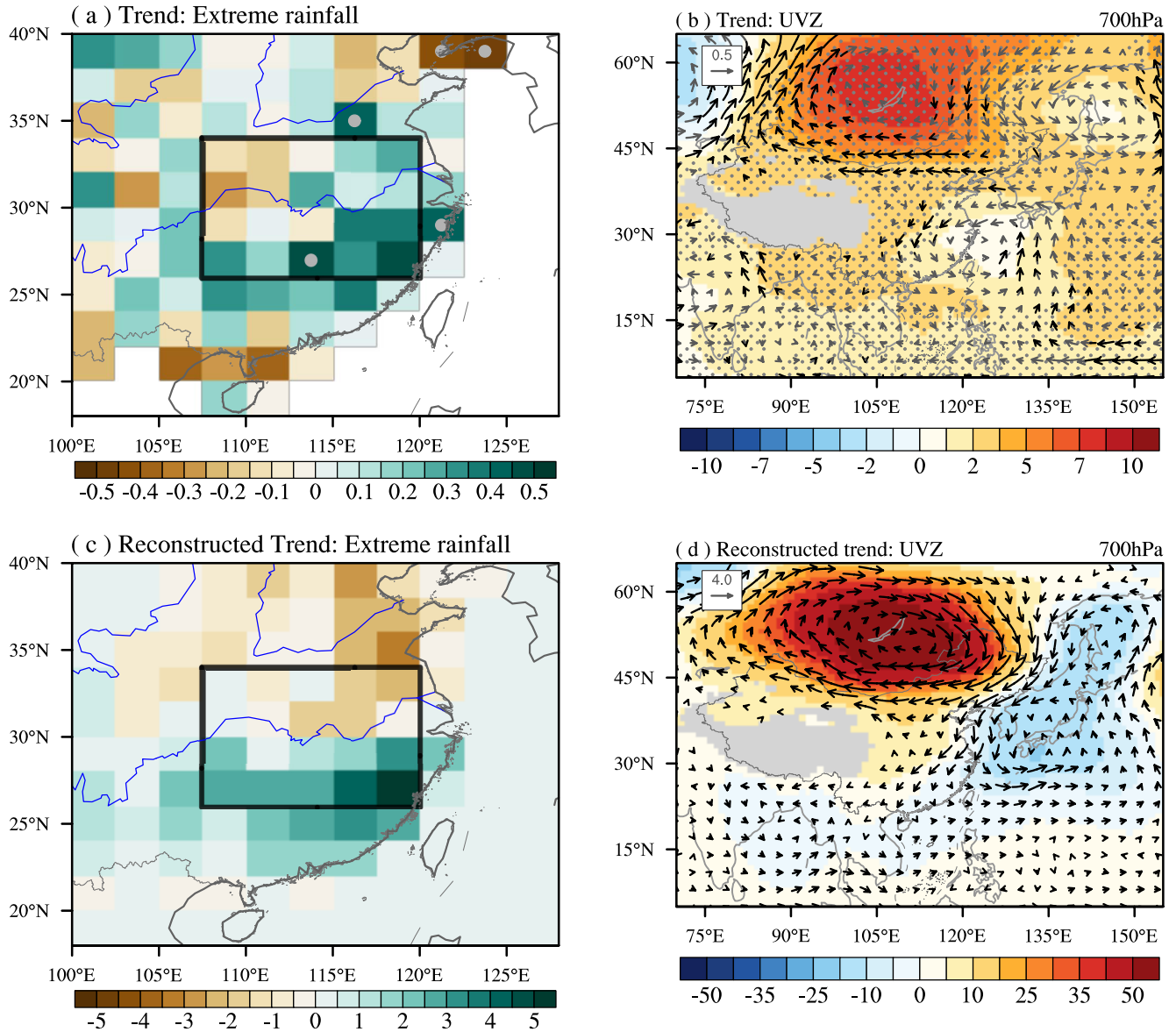

Figure 8. The spatial distribution of long-term trends of (a) local extreme rainfall frequency (units: decade^{-1}) and (b) summer-mean (June and July) circulation (geopotential height, shading, units: gpm decade^{-1}; horizontal wind, vectors, units: m s^{-1} decade $^{-1}$) at 700 hPa. The significant linear trends ($p < 0.1$) of rainfall frequency and geopotential height (wind flow) are highlighted by gray dots (black vectors). The reconstructed long-term trends of (c) local extreme rainfall intensity (units: mm decade^{-1}) and (d) circulation (geopotential height, shading, units: gpm decade^{-1}; horizontal wind, vectors, units: m s^{-1} decade $^{-1}$) using the trends of SP-Cluster 1 and SP-Cluster 3.

the long-term impact of circulation changes on local extreme rainfall, even though the two do not have apparent connections at first sight. Specifically, the long-term changes of circulation imply more (less) frequent SP-Cluster 1 (SP-Cluster 3). As SP-Cluster 1 (SP-Cluster 3) tends to produce more extreme rainfall to the south (north) of the Yangtze River, the circulation changes tend to produce more frequent extreme rainfall to the south of the Yangtze River.

Given the close connection between the typical SPs and extreme rainfall at various timescales, we can better project the future changes in extreme rainfall by weighting the models based on their capability to capture the observed typical SPs in historical simulations. Many previous studies constrained extreme rainfall projections by directly using rainfall-based evaluation metrics (Gründemann et al., 2022; W. Li et al., 2016; B. Tang et al., 2021; Zhao et al., 2022), thus paying less attention to the indispensable processes for extreme rainfall formation. Some recent studies utilized process-oriented (circulation-rainfall relationship) metrics at large-scale but they

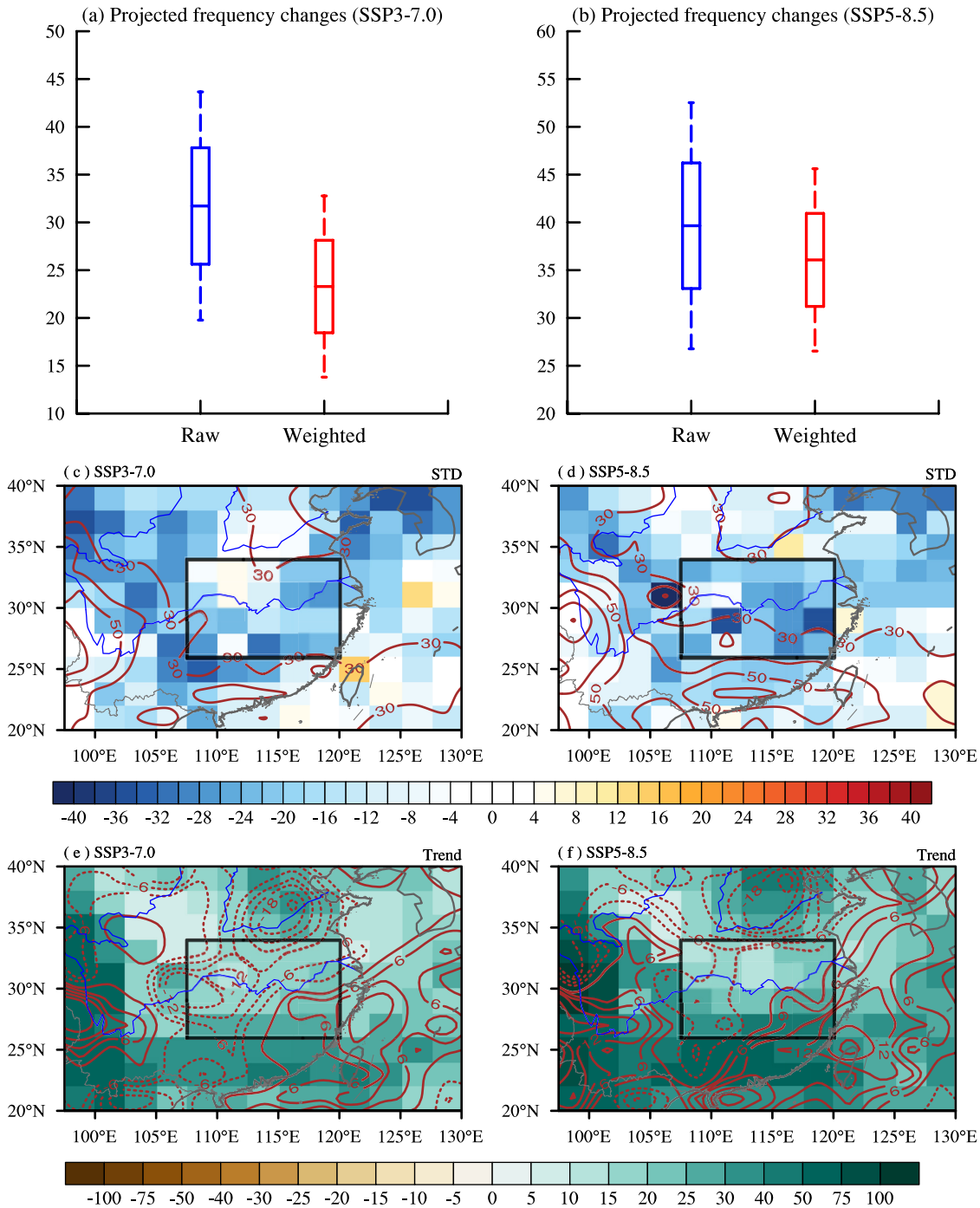

Figure 9. (a, b) Projected future changes (units: %) in extreme rainfall frequency over middle and lower reaches of Yangtze River in different scenarios using the raw (blue) and weighted (red) multi-model ensemble (MME). The boxes indicate the 68%, 95% confidence interval of MME mean. (c, d) The standard deviation (STD; units: %) of projected changes in local extreme rainfall frequency using the raw MME (brown contours) and the percentile changes (shading) using the weighted MME. (e, f) The projected MME mean changes in local extreme rainfall frequency (shading) using the raw MME and the changes (brown contours) using the weighted MME (weighted minus raw).

mainly focused on the mean rainfall projection (F. Li et al., 2022; Wang et al., 2021). Our study proposes a new process-oriented metric to evaluate models' capability in triggering extreme events, and it effectively reduces model uncertainties. Note that the current assessment metric has some uncertainties in capturing a model's bias in extreme rainfall formation. (a) We assign each typical SP in CMIP6 models to a typical SP in observations, and utilize their correlation coefficients to determine the model skill index. However, this algorithm may not fully

capture the model bias, for example, a model could achieve a high skill index even if it merely reproduces a subset of the observed typical SPs. (b) The typical SPs do not encompass all the essential processes for extreme rainfall formation in MLYR during summer. As shown in Figure 4, the reconstructed rainfall using typical SPs exhibits lower magnitudes than the observed rainfall due to other factors such as local convection. Therefore, our method may find better application in investigating the extreme rainfall at mid- and high-latitudes during the cold season where the role of convection is weak and synoptic forcing is strong. In addition, the distinct long-term trends of different typical SPs imply potential changes in the importance of different dynamical regimes in the future. These issues will be investigated in our future research.

Appendix A: Mei-Yu Front Line

The cluster-mean location of the Mei-yu front line is the average of the daily Mei-yu front line at 850 hPa. The Mei-yu front zone is featured by strong meridional gradients of equivalent potential temperature ($|\partial\theta_e/\partial y|$). Following this characteristic of Mei-yu fronts and the method of Y. Li et al. (2018), the locations of daily Mei-yu front lines are detected as follows:

(a) Within the domain of 25–35°N and 107–135°E, we first identify the front zone at each longitude where $|\partial\theta_e/\partial y|$ exceeding 0.04 K km^{-1}. (b) Next, we determine the meridional location of the front line as the mean latitude of the front zone at each longitude. (c) Finally, we only use the daily front line that is zonally continuous to calculate the cluster-mean front line. The zonally continuous front line is defined as: (a) the total number of grids with $|\partial\theta_e/\partial y| > 0.04$ K km^{-1} exceeds 50; (b) the average difference in the mean latitudes between adjacent longitudes is less than 1 (i.e., $\frac{1}{N-1} \times \sum_{0}^{N-2} |\mathrm{lat(i+1)} - \mathrm{lat(i)}| < 1$); and (c) the standard deviation of the mean latitudes is less than 2.0.

Data Availability Statement

The datasets used in this study are available in the public domains: The ERA5 reanalysis data (Hersbach et al., 2023) is available at Copernicus Climate Change Service Climate Data Store (https://cds.climate.copernicus.eu/cdsapp#!/dataset/reanalysis-era5-pressure-levels?tab=form). The gridded rainfall dataset (Wu & Gao, 2013) can be found at https://ccrc.iap.ac.cn/resource/detail?id=228. The CMIP6 data is available at Earth System Grid Federation (https://esgf-node.llnl.gov/search/cmip6/).

Acknowledgments
This study was supported by the National Natural Science Foundation of China (Nos. 41921005, 42230612 and 41905071) and the Research Project for Meteorological Capacity Improvement (23NLTSQ004). Deng is in part supported by the U.S. National Science Foundation through Grant AGS-2032532 and by the U.S. National Oceanic and Atmospheric Administration through Grants NA20OAR4310380 and NA22OAR4310606.

References

Agel, L., & Barlow, M. (2020). How well do CMIP6 historical runs match observed Northeast US Precipitation and extreme precipitation–related circulation? *Journal of Climate*, *33*(22), 9835–9848. https://doi.org/10.1175/JCLI-D-19-1025.1

Agel, L., Barlow, M., Polonia, J., & Coe, D. (2020). Simulation of northeast US extreme precipitation and its associated circulation by CMIP5 models. *Journal of Climate*, *33*(22), 9817–9834. https://doi.org/10.1175/JCLI-D-19-0757.1

Barlow, M., Gutowski, W. J., Gyakum, J. R., Katz, R. W., Lim, Y. K., Schumacher, R. S., et al. (2019). North American extreme precipitation events and related large-scale meteorological patterns: A review of statistical methods, dynamics, modeling, and trends. *Climate Dynamics*, *53*(11), 6835–6875. https://doi.org/10.1007/s00382-019-04958-z

Brunner, L., Lorenz, R., Zumwald, M., & Knutti, R. (2019). Quantifying uncertainty in European climate projections using combined performance-independence weighting. *Environmental Research Letters*, *4*(12), 124010. https://doi.org/10.1088/1748-9326/ab492f

Chen, S., Yang, X. Q., Fang, J., Sun, L., Tao, L., Sang, X., & Yin, M. (2023). Revisiting the East Asian summer monsoon structure: A combined effect of condensational heating and synoptic eddy activities. *Climate Dynamics*, *61*(7–8), 1–17. https://doi.org/10.1007/s00382-023-06763-1

Chen, Y., & Zhai, P. (2015). Synoptic-scale precursors of the East Asia/Pacific teleconnection pattern responsible for persistent extreme precipitation in the Yangtze River Valley. *Quarterly Journal of the Royal Meteorological Society*, *141*(689), 1389–1403. https://doi.org/10.1002/qj.2448

Dai, P., & Nie, J. (2020). A global quasigeostrophic diagnosis of extratropical extreme precipitation. *Journal of Climate*, *33*(22), 9629–9642. https://doi.org/10.1175/JCLI-D-20-0146.1

Davenport, F. V., & Diffenbaugh, N. S. (2021). Using machine learning to analyze physical causes of climate change: A case study of US Midwest extreme precipitation. *Geophysical Research Letters*, *48*(15), e2021GL093787. https://doi.org/10.1029/2021GL093787

Ding, Y. H., & Chan, J. C. L. (2005). The East Asian summer monsoon: An overview. *Meteorology and Atmospheric Physics*, *89*(1–4), 117–142. https://doi.org/10.1007/s00703-005-0125-z

Eyring, V., Bony, S., Meehl, G. A., Senior, C. A., Stevens, B., Stouffer, R. J., & Taylor, K. E. (2016). Overview of the Coupled Model Intercomparison Project Phase 6 (CMIP6) experimental design and organization. *Geoscientific Model Development*, *9*(5), 1937–1958. https://doi.org/10.5194/gmd-9-1937-2016

Gao, X., Schlosser, C. A., O'Gorman, P. A., Monier, E., & Entekhabi, D. (2017). Twenty-first-century changes in US regional heavy precipitation frequency based on resolved atmospheric patterns. *Journal of Climate*, *30*(7), 2501–2521. https://doi.org/10.1175/jcli-d-16-0544.1

Gibson, P. B., Perkins-Kirkpatrick, S. E., & Renwick, J. A. (2016). Projected changes in synoptic weather patterns over New Zealand examined through self-organizing maps. *International Journal of Climatology*, *36*(12), 3934–3948. https://doi.org/10.1002/joc.4604

Gibson, P. B., Uotila, P., Perkins-Kirkpatrick, S. E., Alexander, L. V., & Pitman, A. J. (2016). Evaluating synoptic systems in the CMIP5 climate models over the Australian region. *Climate Dynamics*, *47*(7–8), 2235–2251. https://doi.org/10.1007/s00382-015-2961-y

Gründemann, G. J., van de Giesen, N., Brunner, L., & van der Ent, R. (2022). Rarest rainfall events will see the greatest relative increase in magnitude under future climate change. *Communications Earth & Environment*, *3*(1), 235. https://doi.org/10.1038/s43247-022-00558-8

Hersbach, H., Bell, B., Berrisford, P., Biavati, G., Horányi, A., Muñoz Sabater, J., et al. (2023). ERA5 hourly data on pressure levels from 1940 to present. [Dataset]. Copernicus Climate Change Service (C3S) Climate Data Store (CDS). https://cds.climate.copernicus.eu/cdsapp#!/dataset/reanalysis-era5-pressure-levels?tab=overview

Hu, Y., Deng, Y., Lin, Y., Zhou, Z., Cui, C., & Dong, X. (2021). Dynamics of the spatiotemporal morphology of Mei-yu fronts: An initial survey. *Climate Dynamics*, *56*(9–10), 2715–2728. https://doi.org/10.1007/s00382-020-05619-2

Hu, Y., Deng, Y., Lin, Y., Zhou, Z., Cui, C., Li, C., & Dong, X. (2022). Indirect effect of diabatic heating on Mei-yu frontogenesis. *Climate Dynamics*, *59*(3–4), 851–868. https://doi.org/10.1007/s00382-022-06159-7

Hu, Y., Deng, Y., Zhou, Z., Cui, C., & Dong, X. (2019). A statistical and dynamical characterization of large-scale circulation patterns associated with summer extreme precipitation over the middle reaches of Yangtze River. *Climate Dynamics*, *52*(9–10), 6213–6228. https://doi.org/10.1007/s00382-018-4501-z

Hu, Y., Deng, Y., Zhou, Z., Li, H., Cui, C., & Dong, X. (2019). A synoptic assessment of the summer extreme rainfall over the middle reaches of Yangtze River in CMIP5 models. *Climate Dynamics*, *53*(3–4), 2133–2146. https://doi.org/10.1007/s00382-019-04803-3

Jiang, Y., Zhu, Z., Li, J., Miao, L., & Miao, Z. (2023). Changes of mean and extreme precipitation and their relationship in Northern Hemisphere land monsoon domain under global warming. *International Journal of Climatology*, *43*(12), 5536–5552. https://doi.org/10.1002/joc.8159

Li, C., Zwiers, F., Zhang, X., Li, G., Sun, Y., & Wehner, M. (2021). Changes in annual extremes of daily temperature and precipitation in CMIP6 models. *Journal of Climate*, *34*(9), 3441–3460. https://doi.org/10.1175/JCLI-D-19-1013.1

Li, F., Zhu, Q., Riley, W. J., Yuan, K., Wu, H., & Gui, Z. (2022). Wetter California projected by CMIP6 models with observational constraints under a high GHG emission scenario. *Earth's Future*, *10*(4), e2022EF002694. https://doi.org/10.1029/2022EF002694

Li, J., Zhai, P., Mao, J., Song, L., & Xiao, Q. (2021). Synergistic effect of the 25–60-day tropical and midlatitude intraseasonal oscillations on the persistently severe Yangtze floods. *Geophysical Research Letters*, *48*(20), e2021GL095129. https://doi.org/10.1029/2021GL095129

Li, W., Jiang, Z., Xu, J., & Li, L. (2016). Extreme precipitation indices over China in CMIP5 models. Part II: Probabilistic projection. *Journal of Climate*, *29*(24), 8989–9004. https://doi.org/10.1175/JCLI-D-16-0377.1

Li, X., & Lu, R. (2017). Extratropical factors affecting the variability in summer precipitation over the Yangtze River basin, China. *Journal of Climate*, *30*(20), 8357–8374. https://doi.org/10.1175/JCLI-D-16-0282.1

Li, X., Lu, R., & Wang, X. (2023). Effect of large-scale circulation anomalies on summer rainfall over the Yangtze River basin: Tropical vs. Extratropical. *Journal of Climate*, 1–33. https://doi.org/10.1175/JCLI-D-22-0717.1

Li, Y., Deng, Y., Yang, S., & Zhang, H. (2018). Multi-scale temporospatial variability of the East Asian Meiyu-Baiu fronts: Characterization with a suite of new objective indices. *Climate Dynamics*, *51*(5–6), 1659–1670. https://doi.org/10.1007/s00382-017-3975-4

Loikith, P. C., & Broccoli, A. J. (2015). Comparison between observed and model-simulated atmospheric circulation patterns associated with extreme temperature days over North America using CMIP5 historical simulations. *Journal of Climate*, *28*(5), 2063–2079. https://doi.org/10.1175/jcli-d-13-00544.1

Ohba, M., Arai, R., Sato, T., Imamura, M., & Toyoda, Y. (2022). Projected future changes in water availability and dry spells in Japan: Dynamic and thermodynamic climate impacts. *Weather and Climate Extremes*, *38*, 100523. https://doi.org/10.1016/j.wace.2022.100523

O'Neill, B. C., Tebaldi, C., Vuuren, D. P. V., Eyring, V., Friedlingstein, P., Hurtt, G., et al. (2016). *The scenario model intercomparison project (ScenarioMIP) for CMIP6* (Vol. 9, pp. 3461–3482). Geoscientific Model Development. https://doi.org/10.5194/gmd-9-3461-2016

Prein, A. F., & Mearns, L. O. (2021). US extreme precipitation weather types increased in frequency during the 20th century. *Journal of Geophysical Research: Atmospheres*, *126*(7), e2020JD034287. https://doi.org/10.1029/2020JD034287

Sampe, T., & Xie, S. P. (2010). Large-scale dynamics of the meiyu-baiu rainband: Environmental forcing by the westerly jet. *Journal of Climate*, *23*(1), 113–134. https://doi.org/10.1175/2009jcli3128.1

Tang, B., Hu, W., & Duan, A. (2021). Future projection of extreme precipitation indices over the Indochina Peninsula and South China in CMIP6 models. *Journal of Climate*, *34*(21), 8793–8811. https://doi.org/10.1175/JCLI-D-20-0946.1

Tang, Y., Huang, A., Wu, P., Huang, D., Xue, D., & Wu, Y. (2021). Drivers of summer extreme precipitation events over East China. *Geophysical Research Letters*, *48*(11), e2021GL093670. https://doi.org/10.1029/2021GL093670

Taylor, G. P., Loikith, P. C., Aragon, C. M., Lee, H., & Waliser, D. E. (2023). CMIP6 model fidelity at simulating large-scale atmospheric circulation patterns and associated temperature and precipitation over the Pacific Northwest. *Climate Dynamics*, *60*(7–8), 2199–2218. https://doi.org/10.1007/s00382-022-06410-1

Wang, L., Qian, Y., Leung, L. R., Chen, X., Sarangi, C., Lu, J., et al. (2021). Multiple metrics informed projections of future precipitation in China. *Geophysical Research Letters*, *48*(18), e2021GL093810. https://doi.org/10.1029/2021GL093810

Ward, J. H., Jr. (1963). Hierarchical grouping to optimize an objective function. *Journal of the American Statistical Association*, *58*(301), 236–244. https://doi.org/10.1080/01621459.1963.10500845

Wu, J., & Gao, X. J. (2013). A gridded daily observation dataset over China region and comparison with the other datasets [Dataset]. Chinese Journal of Geophysics, *56*(4), 1102–1111. http://www.geophy.cn//article/doi/10.6038/cjg20130406

Xu, H., Chen, H., & Wang, H. (2021). Future changes in precipitation extremes across China based on cmip6 models. *International Journal of Climatology*, *42*(1), 635–651. https://doi.org/10.1002/joc.7264

Xu, X., Huang, A., Huang, D., Zhang, Y., Gu, C., Cai, S., et al. (2023). What are the dominant synoptic patterns leading to the summer regional hourly extreme precipitation events over central-eastern Tibetan Plateau and Sichuan Basin? *Geophysical Research Letters*, *50*(5), e2022GL102342. https://doi.org/10.1029/2022GL102342

Xu, Z., Yang, X. Q., Tao, L., & Sun, L. (2023). Impact of anomalous Eurasian blocking activities on the East Asian Meiyu rainfall. *Climate Dynamics*, *61*(7–8), 1–20. https://doi.org/10.1007/s00382-023-06735-5

Zhang, C., Huang, X., Fei, J., Luo, X., & Zhou, Y. (2021). Spatiotemporal characteristics and associated synoptic patterns of extremely persistent heavy rainfall in southern China. *Journal of Geophysical Research: Atmospheres*, *126*(1), e2020JD033253. https://doi.org/10.1029/2020JD033253

Zhang, F., Zhang, Q., Sun, J., & Xu, J. (2023). Convection initiation during the Meiyu environment in the Yangtze-Huai River basin of China. *Journal of Geophysical Research: Atmospheres*, *128*(9), e2022JD038077. https://doi.org/10.1029/2022JD038077

Zhang, S., Chen, Y., Luo, Y., Liu, B., Ren, G., Zhou, T., et al. (2022). Revealing the circulation pattern most conducive to precipitation extremes in Henan Province of North China. *Geophysical Research Letters*, *49*(7), e2022GL098034. https://doi.org/10.1029/2022GL098034

Zhao, J., He, S., & Wang, H. (2022). Historical and future runoff changes in the Yangtze River Basin from CMIP6 models constrained by a weighting strategy. *Environmental Research Letters*, *17*(2), 024015. https://doi.org/10.1088/1748-9326/ac3f61

Zhao, S., Deng, Y., & Black, R. X. (2016). Warm season dry spells in the central and eastern United States: Diverging skill in climate model representation. *Journal of Climate*, *29*(15), 5617–5624. https://doi.org/10.1175/JCLI-D-16-0321.1

Zhao, S., Deng, Y., & Black, R. X. (2017). A dynamical and statistical characterization of US extreme precipitation events and their associated large-scale meteorological patterns. *Journal of Climate*, *30*(4), 1307–1326. https://doi.org/10.1175/JCLI-D-15-0910.1

Zhu, Z., Feng, Y., Jiang, W., Lu, R., & Yang, Y. (2023). The compound impacts of sea surface temperature modes in the Indian and North Atlantic oceans on the extreme precipitation days in the Yangtze River Basin. *Climate Dynamics*, *61*(7–8), 1–15. https://doi.org/10.1007/s00382-023-06733-7